Mechanics of Paper-Folded Origami: A Cautionary Tale

Steven W. Grey[a,*], Fabrizio Scarpa[a] and Mark Schenk[a]

[a]Bristol Composites Institute (ACCIS), Department of Aerospace Engineering, University of Bristol, BS8 1TR, United Kingdom

ARTICLE INFO

Keywords:
Engineering Origami
Self-Stress
Experimental Origami
Miura-ori

ABSTRACT

Folded paper has a long history in origami artwork and is used by engineers to rapidly prototype designs of adaptive structures and mechanical metamaterials. However, engineers should be cautious when using paper to investigate the mechanical properties of origami structures. We show that the non-linear, pseudo-plastic behaviour of paper folds complicates the modelling of the mechanical properties of an origami structure. However, this pseudo-plastic behaviour could also present a new design space to tailor the mechanical properties of origami by controlling the rest angles of the folds.

1. Introduction

Paper has been the material of choice for origami artists looking to create complex masterpieces since the first recorded origami in 6th century Japan [23]. Paper has obvious benefits, with a low bending stiffness enabling easy folding and bending of the material, to achieve a wide variety of shapes [14]. These properties have also enabled origami engineers to rapidly prototype adaptive structures and mechanical metamaterials, facilitating communication [29, 18, 9] and validation [5, 25, 12, 10].

However, engineers should use paper with caution as it can exhibit unexpected and unpredictable mechanical properties. Paper is manufactured from a mat of wood pulp, making it a randomly orientated fibre reinforced composite with anisotropic properties [1]. This pulp is then pulled through rollers under tension in order to flatten it, inducing a directionality to the material, and thus making paper stiffer and stronger in one direction. Once the paper is folded into an origami structure, further changes happen to its mechanical properties. Each successive folding cycle damages it, effectively 'delaminating' the paper at the fold and impacting the mechanical properties [3, 19].

Furthermore, the rest angle of each individual fold may also affect the global properties of an origami structure. After forming a single fold by creasing a piece of paper, it will assume a natural rest angle; subsequently flattening the fold again will cause the paper to rest at another—in essence, the fold rest angle depends on its folding history. An origami structure consists of an interconnected set of folds, each with a specific rest angle. The kinematics of the origami pattern will often prevent each fold from assuming its rest angle, resulting in a self-stressed state, which can influence the mechanical behaviour of the structure [30, 25, 4, 27, 16, 31].

This article initially focuses on the stiffness of a single paper fold throughout the folding process. Next, Section 3 considers how some of the peculiarities of paper folds influence the behaviour of an origami structure. Finally, Section 4 draws conclusions on the use of paper to investigate mechanical properties of engineering origami structures.

*Corresponding author
steven.grey@bristol.ac.uk (S.W. Grey)
ORCID(s): 0000-0003-2344-2031 (S.W. Grey)

2. Single Paper Fold

In modelling origami structures, the folds are often simplified to linear torsional springs in order to focus on the global mechanical response. However, when using paper models to experimentally validate such structural analyses [10], the complexity of paper folds cannot be overlooked.

2.1. Experimental Method

Myriad techniques have been used to determine the properties of a single fold. The fold stiffness of paperboard for packaging can be measured using indentation at the fold [20, 21] or a cantilever with the fold at the root [3, 19, 11], reflecting the packaging manufacturing process. These methods use the reaction force at the point of actuation to derive the fold stiffness, but ignore the effect of the material between the folds bending. Francis et al. [8] use an 'L'-shaped cantilever, fully fixed on one arm and actuated at the other, with the measured fold in the middle. The difference between the fold angle change and the change in the angle subtended between the fixed and actuated ends of the 'L' indicates the influence of facet bending on the measured reaction force. However, the contributions of the fold rotation and the facet bending are not separated.

Clamping the material either side of the fold and uniaxially displacing the clamps to open or close the fold produces a reaction force due to both the material bending and the torsional stiffness of the fold. By measuring the fold angle and modelling the facet bending, the respective contributions to the measured reaction force can be identified [15, 28]. However, this approach requires accurate knowledge of the material flexural properties to model the facet deformations, which may not be available for paper.

Boatti et al. [2] introduce an extra fold on either side of the main fold of interest; this alleviates the facet bending and also increases the reaction load, making experimental design easier. However, if the fold stiffness is non-linear it cannot be obtained due to the differing rotational displacements of each fold. To avoid this, Pradier et al. [22] use a hinge joint with a low stiffness tape. Additionally, to eliminate the need to model the facet bending it can be reinforced with extra material [17] or by including folded tabs to increase the second moment of area [7].

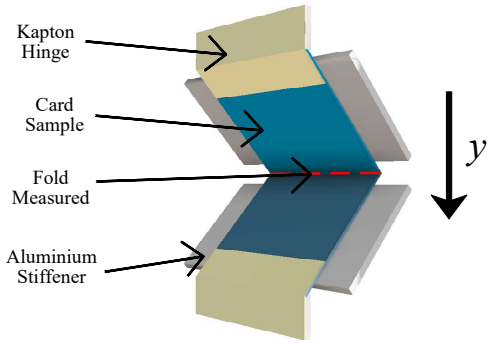

Figure 1: Experimental set-up for single fold stiffness.

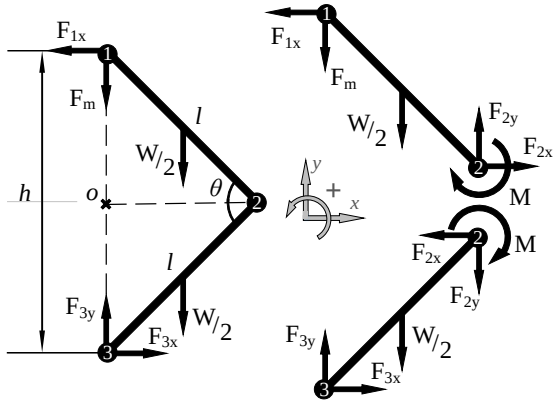

Figure 2: Forces and moments on a single fold, assuming the facets do not deform and perfect hinges at the top and bottom.

In this work Aluminium stiffeners are added to the paper card to increase the facet bending stiffness by two orders of magnitude; see Figure 1. The folded samples are opened and closed in a Shimadzu uniaxial testing machine at 1 mm/s and the reaction force is measured using a 10 N load cell. The hinges on the top and bottom are made from 0.025 mm thick Kapton film for its low flexural stiffness.

The fold moment-angle relationship is calculated from the measured force-displacement response. From equilibrium of the forces and moments in Figure 2 the moment at the fold, M, is:

$$M = l \cos\left(\frac{\theta}{2}\right)\left(\frac{W}{2} + F_m\right) \tag{1}$$

in terms of the length of the facet, l, the fold angle, θ, the combined weight of both facets, W, and the measured reaction force F_m. The torsional stiffness of the fold is then obtained numerically from the gradient of the moment with respect to the fold angle.

2.2. Experimental Results

The material used in the experiments is 300 gsm Canford card with a measured Young's modulus and Poisson's ratio of $E_{11} = 6.1$ GPa and $\nu_{12} = 0.4$ in the grain direction and $E_{22} = 2.3$ GPa and $\nu_{21} = 0.17$ perpendicular to the grain (determined using the ASTM D828-16 test standard). Folded samples are manufactured by laser cutting a 60×30 mm rectangle, with a perforated fold line (removing 2 mm of material every 2 mm) dividing it into two squares. Five samples with their fold aligned to the grain and five perpendicular to the grain, are each subjected to five cycles from flat ($\theta = 180°$) to folded ($\theta = 0°$) and back to flat again.

The results showed that the grain direction has no significant impact on the torsional stiffness of the fold; this in contrast to the Young's modulus. Therefore, for this article we assume that the fold properties are independent of the grain direction. This could be due to the perforation process removing material, limiting the difference between aligned and perpendicular samples, or damage sustained during the folding process minimising the effect of fibre alignment.

Figure 3a combines both the aligned and perpendicular samples to show the experimental scatter for the induced moment at the fold line for the fifth loading cycle. Each successive cycle reduces the experimental scatter; by the fifth cycle the response has become consistent from cycle to cycle, producing a more repeatable response. The measured fold response is highly non-linear and shows a significant hysteresis, suggesting a 'plastic' deformation in the fold caused by damage induced within the paper. The response is most non-linear and most variable from sample to sample on the first cycle of loading; hence, the folds are exposed to five cycles to minimise this variability.

This plastic deformation manifests in the form of the natural rest angles of a fold. If the fold is creased it will rest at one angle; if that fold is then flattened again, it will assume another angle. This is replicated using ten additional samples to obtain characteristic rest angles for the Canford card; the experimental scatter of these rest angles across five cycles of folding can be found in the bars centred on $\theta \approx 52°$ and $\theta \approx 158°$ in Figure 3a. As these represent energy minima of the fold, they should both coincide with the equilibrium points along the curve where there is zero moment at the fold; however, due to the experiment being unable to exactly reach 0° and 180° there is a slight discrepancy. This highlights another complexity of modelling paper folds in origami: the rest angles are strongly dependent on the deformation history of the fold.

Numerically differentiating the moment with respect to the fold angle yields the torsional stiffness profile of the fold. To minimise the noise generated, a moving window of five degrees either side of the target angle is used to fit a linear gradient to the mean moment. This is then reported as the linearised local torsional stiffness for that fold angle; see Figure 3b. The resulting stiffness profile is highly non-linear; to minimise the error in the linear stiffness near both rest angles, a fold stiffness of 2 Nmm/rad is chosen for use in the Finite Element Analysis (FEA) and rigid origami models

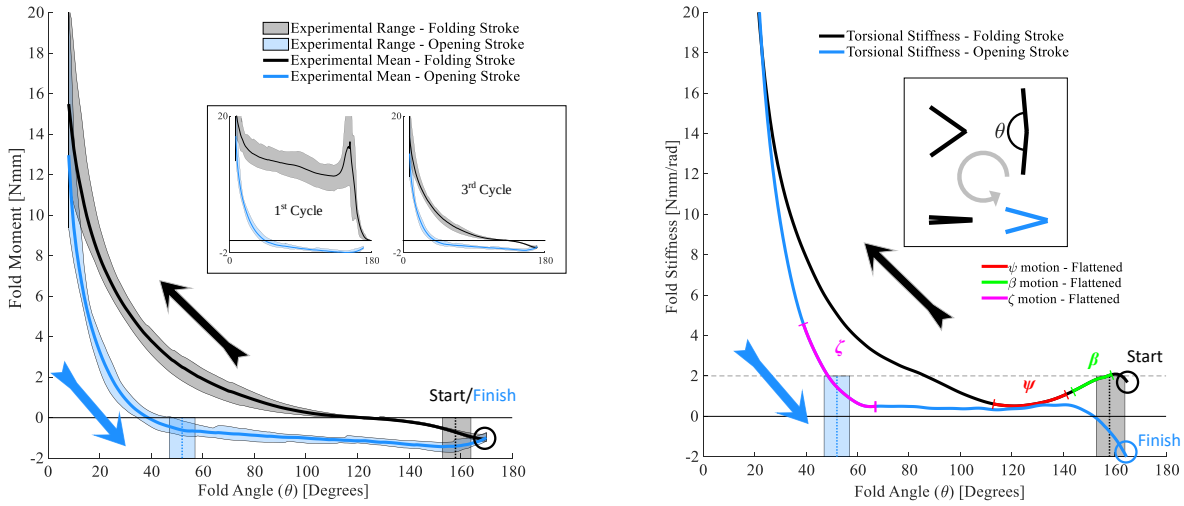

(a) (b)

Figure 3: The results of the single fold experiments on the fifth cycle of folding. The blue and grey bars represent the experimentally obtained rest angle of the folds when folded and unfolded respectively. (a) The moment angle relationship for the fifth cycle (inset first and third cycles); the experimental range represents minimum and maximum moments across all of the samples tested. (b) Numerically differentiating the moment gives the torsional stiffness of the fold. The range of angles (ζ, ψ, β) of the folds during the compression of the Miura-ori tubes described in Section 3.2 are highlighted.

discussed in Section 3. However, this single linear stiffness can only have a limited validity, with the direction of folding, folding history, and the current fold angle all contributing to the stiffness of each individual fold. This number of variables inevitably leads to a high degree of uncertainty in the mechanical properties of the overall origami structure.

3. Folded Paper in Origami Structures

Paper origami structures consist of an interacting network of such non-linear folds. These determine the minimum energy configuration of the overall structure as well as its mechanical properties.

This paper focuses on the Miura-ori tube [6, 10], which is based on the unit cell shown in Figure 4. A second unit cell is mirrored in the xy-plane; these are mated together and tessellated to form a tube. The geometric parameters used in this work are $a = b = 30$ mm and $\alpha = 60°$, as defined in Figure 4. Assuming that the facets do not deform (*i.e.* rigid origami), the Miura-ori tube has a single degree of freedom, offering axial extension and compression of the tube.

Physically realisable paper folds in Miura-ori tubes exhibit a rest angle which depends on the history of folding, as explored in Section 2.2. Kinematically, the folds in the Miura-ori tube have different angles, which means that the folds cannot all assume their preferred rest angle. Instead, the tube settles into a self-stressed, minimum-energy, equilibrium configuration where all folds are offset from their natural rest angle. The concept of rest angles differing from the initial configuration is not new, many reduced order models of origami [30, 25, 4, 27, 16] allow for this principle, but the influence of this on the properties of physical paper models has not been explored. We highlight the influence of the self-stressed state, generated by using physically appropriate rest angles dependent on the folding history, on the behaviour of Miura-ori tubes. These are compared to initially stress-free tubes with the same initial configuration.

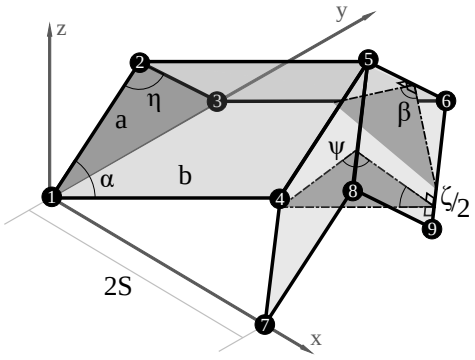

Figure 4: Geometric parameters of Miura-ori unit cell.

3.1. Folded Origami at Rest

To determine the minimum energy state of an origami structure, the simplest approach is to use the rigid origami assumption [26]. In this purely kinematic description of origami the Miura-ori tube has a single degree of freedom. The internal energy, U, can be obtained using:

$$U = \frac{1}{2}\sum_{i=1}^{N} k_i \left(\theta_i - \theta_{i0}\right)^2 \tag{2}$$

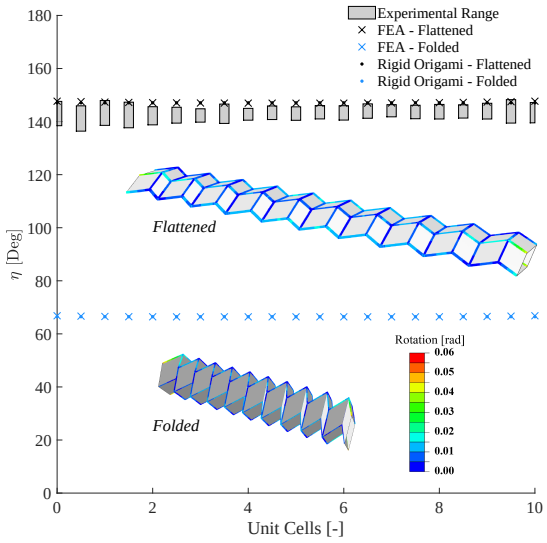

Figure 5: Resting state of a Miura-ori tube (inset; colours represent change in fold angle measured by the rotation of the connector elements representing the fold) obtained from the experimental, numerical, and rigid origami models. The experimental data consists of five samples each subjected to five cycles. Unit cells are defined from zero on the left of the left most cell to ten on the right of the right most cell.

where N is the number of folds and k_i, θ_i, and θ_{i0} are the torsional stiffness, the fold angle, and the rest angle for a given fold i respectively. The minimum energy state determines the rest configuration of the origami structure; given its single degree of freedom, this is uniform across the Miura-ori tube.

The FE modelling captures facet deformations, thus allowing for a non-uniform rest state along the length of the tube. The FEA model is developed in ABAQUS/Standard using S4R shell elements for the facets (25×25 elements per facet) and CONN3D2 elements as linear torsional springs on the folds. These springs can be given an offset from the initial position, simulating the rest angles of each individual fold. To aid convergence in ABAQUS/Standard, the output of the rigid origami model is used as the initial position of the structure, thereby minimising the deformations. The properties used in the FEA model are representative of the material used in Section 2.2. Comparing models with orthotropic facets to those with effective isotropic facet properties show minimal difference, therefore, isotropic properties are used. Comparing the rigid origami model with the numerical FEA model isolates the effect of the facets deforming on the overall shape of the rest configuration. The numerical model shows a largely uniform response, as illustrated in Figure 5, suggesting that the self-stress in the tubes is insufficient to generate significant facet deformations.

The self-stressed equilibrium configuration is also investigated experimentally. Miura-ori tubes with ten unit cells are manufactured from the 300 gsm Canford card analysed in Section 2; each tube consists of two halves, which are cut and perforated in the same way as the single fold samples. These halves are pre-folded before being bonded together using double sided adhesive tape attached to tabs on one of the halves. In preparation for the test, the completed tube is first fully compressed and then fully extended in the x-direction (as defined in Figure 4). This procedure ensures that all folds start from either fully folded or flattened configuration, allowing the measured rest angles from the single fold tests to be used in the calculations. The tube assumes a "*flattened*" state after it has been fully extended and allowed to rest, and takes a "*folded*" state after it has been fully compressed. The folded tube has a much lower stiffness meaning that handling the sample influences the geometry measured; therefore, only flattened experimental data is presented. The external geometry of the tube is captured as a point cloud by a laser scanner. This point cloud is processed to find the fold lines and, assuming the fold lines remain straight, fits these to a vector using a least squares regression. Finding the angle between the vectors for the front and back parallel folds allows for the definition of the angle η, which characterises the state of the tube along its length.

The experimentally derived rest angles suggest that the rigid origami and FEA models both slightly overestimate η (*i.e.* a longer tube). This could be due to manufacturing misalignments during the assembly of the tubes; however, one would expect these errors to be random, increasing the scatter of the experimental results instead of causing an underestimation of the model. Instead, more likely causes of the systematic error are the assumed constant torsional stiffness of the folds, or uncertainty in the rest angles of the folds.

3.2. Folded Origami in Motion

After determining the equilibrium configuration of the Miura-ori tube, we next assess the extent to which the state of self-stress affects its mechanical properties. We focus on the axial stiffness of the Miura-ori tube; this deformation mode minimises the facet deformations, simplifying the structural response, and can be replicated experimentally.

3.2.1. Axially Compressed Miura-ori Tubes

Focusing on a system with minimal facet deformations enables the use of a kinematic rigid origami model to rapidly evaluate different combinations of fold rest angles. The accuracy of rigid origami for calculating the axial stiffness of a tube is validated by comparing to FEA simulations and experimental results for axial compression.

The experiments consist of five tubes with five unit cells manufactured using the method described previously. The aim is to obtain a force-displacement response for the compression of a Miura-ori tube starting from both the "flattened" and the "folded" resting configurations. After assuming its rest configuration, the Miura-ori tube is placed upright onto a smooth glass plate which is mounted into a uniaxial testing machine. A second glass plate is lowered to compress the tube between the plates, and a 10 N load cell records the reaction force; this is repeated for five cycles. The smooth glass minimises the friction between the tube and the plates

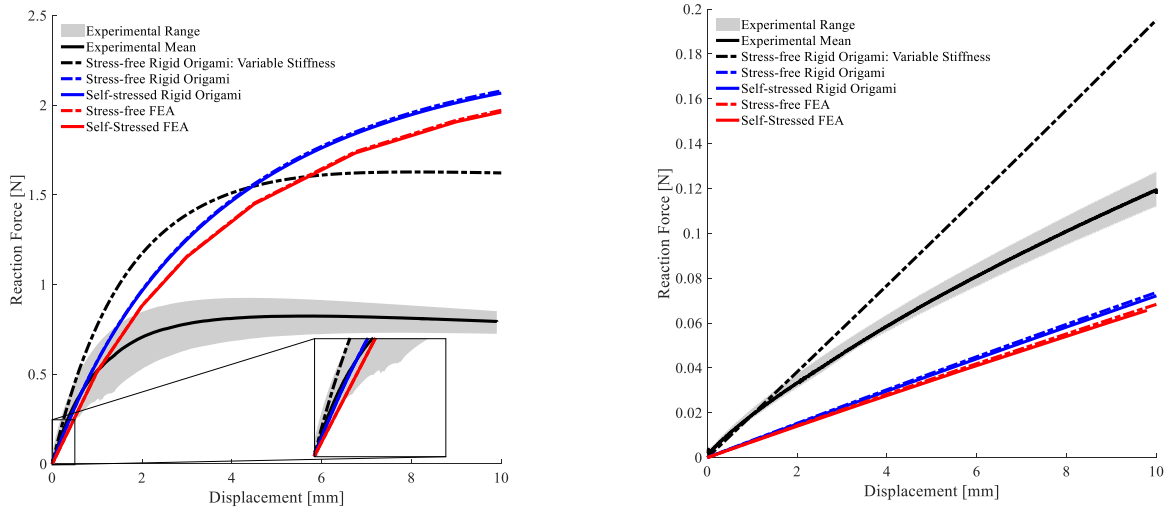

Figure 6: Force displacement results for experimental, numerical, and rigid origami models. The Miura-ori tube is either (a) fully extended or (b) fully compressed, and allowed to assume its equilibrium configuration; initial lengths are respectively 260 mm and 120 mm. The experimental scatter represents the minimum and maximum across the five samples tested on their fifth cycle of testing, the serration visible in (a) is due to experimental noise. Corresponding fold rotations for the flattened tube are highlighted in Figure 3b and are negligible for the folded tube over the displacement measured.

with the aim of allowing the ends of the tube to deform freely as the tube is compressed.

Using the rigid origami kinematics, the axial force F and axial stiffness K can be calculated using Castigliano's second theorem,

$$F = \frac{dU}{dx} = \sum_{i=1}^{N} \left(\frac{dg}{d\theta_i} \frac{d\theta_i}{dx} \right) = \sum_{i=1}^{N} \left(M_i \frac{d\theta_i}{dS} \frac{dS}{dx} \right) = \frac{1}{2n} \sum_{i=1}^{N} M_i \frac{d\theta_i}{dS} \tag{3}$$

where U is the internal strain energy, which is a nonlinear function $g(x)$ of the extension/compression x of the tube. The rate of change of g with respect to fold angle θ_i is the moment M_i induced at the fold; for folds with a linear stiffness, $M_i = k_i \left(\theta_i - \theta_{i0}\right)$, where θ_{i0} is the natural rest angle of the fold. The half-width S of a unit cell (see Figure 4) can be written in terms of the tube extension and compression x, the number of unit cells in the tube n, and the initial dimension S_0,

$$S = \frac{x}{2n} + S_0 \tag{4}$$

This enables the axial force on the Miura-ori to be expressed in terms of the moments M_i at the folds, and the unit cell kinematics $(d\theta_i/dS)$ [24]. Differentiating again with respect to x gives the axial stiffness of the tube, here presented for a linear fold stiffness:

$$K = \frac{1}{(2n)^2} \sum_{i=1}^{N} k_i \left(\left(\theta_i - \theta_{i0}\right) \frac{d^2\theta_i}{dS^2} + \left(\frac{d\theta_i}{dS} \right)^2 \right) \tag{5}$$

The rigid origami and numerical models show similar force-displacement responses for the Miura-ori tube; see Figure 6. This is true for tubes compressed from both a flattened and folded rest state, suggesting that facet deformations are minimal and that a rigid origami model is sufficient. However, the correlation of these models with the experimental results is poor. This difference can be attributed in part to the highly non-linear nature of the fold stiffness, whereas the FE and rigid origami calculations use a constant fold stiffness of 2 Nmm/rad on each fold. Despite the poor correlation, the models do capture the order of magnitude difference in axial stiffness between the two initial configurations of the Miura-ori tube; this difference is driven by the unit cell geometry.

Using the measured stiffness profile in Figure 3b, an incremental fold moment can be calculated for the range of motion of the folds,

$$M_j = M_{j-1} + k_j \left(\theta_{j+1} - \theta_j\right) \tag{6}$$

where for increment j the moment, stiffness, and angle of the fold are given by M_j, k_j, and θ_j respectively. This better captures the softening observed in the Figure 6a.

However, both the flattened and folded tubes show a higher reaction force than is observed experimentally. This could be because the experiments on a single fold used to generate the fold stiffness start from a fully flattened or folded position, whereas the folds in the tubes begin from a partially folded state which could lead to a different rest state or even different fold stiffness. Additionally, the stiffness of the flattened tube is sensitive to the initial folded state, which itself depends on the fold stiffness and rest angles that have an inherent uncertainty. Further, the low stiffness observed in

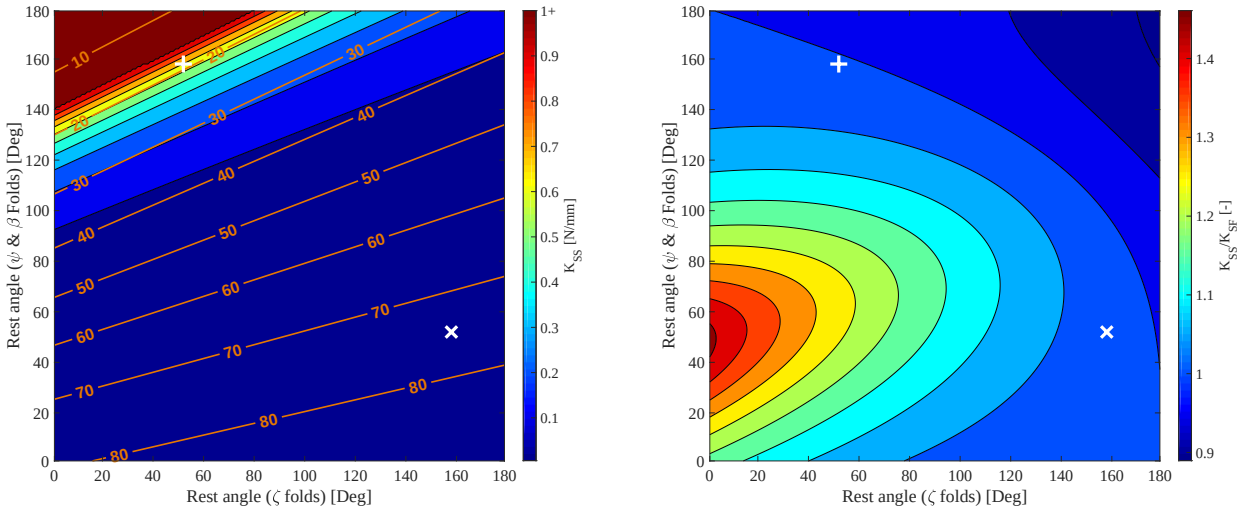

(a) (b)

Figure 7: (a) Axial stiffness of five unit cell Miura-ori tubes calculated using rigid origami for a range of rest angles. Labelled contours represent the corresponding equilibrium configuration, defined by angle $\zeta/2$. The two experimental conditions, "folded" after compression ($\times$), and "flattened" after extension ($+$), are marked. (b) Ratio between the axial stiffness of the tube with (K_{SS}) and without (K_{SF}) self stress in the folds for the same initial configuration.

Figure 6b means it is more susceptible to the effects of self-weight, which is not captured in the rigid origami model (although incorporated in the FE simulations). The difficulty in replicating the response of the physical paper models illustrates the complexities and limitations of using paper when exploring the physical properties of origami structures.

3.2.2. Exploring Rest Angles

The two initial configurations of the Miura-ori tube are the result of different fold rest angles due to the folding history: when fully compressed, the folds on the mirror plane (ζ) are at 180°, and the other folds (β, ψ) are at 0°; and *vice versa* for the fully extended tube.

Assuming that the rest angles may be tailored, the axial stiffness of the tubes can be calculated for a range of fold rest angles. Figure 7a shows the axial stiffness of the Miura-ori tube, as well as the corresponding minimum-energy configuration, for varying fold rest angles (all dimensions as described previously; fold stiffness of 2 Nmm/rad). The two equilibrium configurations for the paper models investigated are marked; note the order of magnitude difference in axial stiffness.

The axial stiffness is not only determined by the geometric configuration, but also by the state of self-stress due to incompatible rest angles of the folds. The ratio of the axial stiffness of the Miura-ori tube with and without self-stress is shown in Figure 7b. For the selected geometry the difference in stiffness can be up to 50%. However, for the two sets of rest angle observed in the card samples, the influence of the self-stress is minimal; therefore, the models in Figure 6 show no noticeable difference between the self-stressed and stress-free models.

The difference between the stiffness of the self-stressed and stress-free tubes also depends on the geometry of the unit cell. For instance, increasing the facet angle to $\alpha = 75°$ significantly increases the effect of self-stress, potentially providing a stiffening of over 500%.

4. Conclusions

Paper is low-cost and widely available in a range of styles and qualities which, along with its ability to easily form compliant hinges, makes it ideal for rapidly prototyping origami models. However, as paper is comprised of a slightly aligned mat of natural fibres it hides complex properties. The fold stiffness characteristics will also depend on the specific material used, and the type of crease (*e.g.* perforation, hemming, scoring) introduced in the paper.

We show how the non-linear stiffness of folded paper can lead to significant errors in the modelling of the mechanical properties of origami structures, where usually a constant fold stiffness is assumed. This means that an origami engineer looking to quantitatively validate a model of an adaptive structure or mechanical metamaterial should be cautious before using paper as a material for prototyping. A particular challenge is to determine the rest angles of the folds, which determine the initial, minimum energy, configuration of the origami structure. Crucially, the rest angle and associated stiffness depends on the loading history of the fold. For future investigations of origami structures, other prototyping materials such as polymer sheets [13] with more linear response are recommended.

However, the rest angles could also provide an opportunity to expand the design space of origami. Selecting the rest angles of the folds means that the uniaxial stiffness of

the Miura-ori tube can be tailored; an interesting avenue for future work would be to investigate how this influences the energy absorption capabilities of the structure. Specially designed torsional springs could be used to select the rest configuration and tune the stiffness or energy absorbing characteristics of the system, leading to a wider range of potential applications of origami.

Acknowledgements

This work was supported by the Engineering and Physical Sciences Research Council (EPSRC) through the ACCIS Doctoral Training Centre [grant number EP/G036772/1].are available at the University of Bristol data repository, data.bris, at https://doi.org/10.5523/bris.3gzjg4hdyg4te2t5148ulmh5a7.

References

[1] Baum, G.A., 1984. The Elastic Properties of Paper: A Review. Technical Report 25. The Institute of Paper Chemistry, Appleton, Wisconsin.

[2] Boatti, E., Vasios, N., Bertoldi, K., 2017. Origami Metamaterials for Tunable Thermal Expansion. Advanced Materials 29, 1700360. doi:10.1002/adma.201700360.

[3] Borgqvist, E., Wallin, M., Tryding, J., Ristinmaa, M., Tudisco, E., 2016. Localized Deformation in Compression and Folding of Paperboard. Packaging Technology and Science 29, 397–414. doi:10.1002/pts.2218.

[4] Brunck, V., Lechenault, F., Reid, A., Adda-Bedia, M., 2016. Elastic theory of origami-based metamaterials. Physical Review E - Statistical, Nonlinear, and Soft Matter Physics 93, 1–14. doi:10.1103/PhysRevE.93.033005.

[5] Dudte, L.H., Vouga, E., Tachi, T., Mahadevan, L., 2016. Programming curvature using origami tessellations. Nature Materials 15, 583–588. doi:10.1038/nmat4540.

[6] Filipov, E., Tachi, T., Paulino, G.H., 2015. Origami tubes assembled into stiff, yet reconfigurable structures and metamaterials. Proceedings of the National Academy of Sciences 112, 12321–12326. doi:10.1073/pnas.1509465112.

[7] Filipov, E.T., Redoutey, M., 2018. Mechanical characteristics of the bistable origami hypar. Extreme Mechanics Letters 25, 16–26. doi:10.1016/j.eml.2018.10.001.

[8] Francis, K.C., Blanch, J.E., Magleby, S.P., Howell, L.L., 2013. Origami-like creases in sheet materials for compliant mechanism design. Mechanical Sciences 4, 371–380. doi:10.5194/ms-4-371-2013.

[9] Gillman, A., Fuchi, K., Buskohl, P.R., 2018. Truss-based nonlinear mechanical analysis for origami structures exhibiting bifurcation and limit point instabilities. International Journal of Solids and Structures 0, 1–14. doi:10.1016/j.ijsolstr.2018.05.011.

[10] Grey, S.W., Scarpa, F., Schenk, M., 2019. Strain Reversal in Actuated Origami Structures. Physical Review Letters 123, 025501. doi:10.1103/PhysRevLett.123.025501.

[11] Huang, H., Hagman, A., Nygårds, M., 2014. Quasi static analysis of creasing and folding for three paperboards. Mechanics of Materials 69, 11–34. doi:10.1016/j.mechmat.2013.09.016.

[12] Ivashtenko, O., Kofman, P., Golubov, O., Maizelis, Z., 2019. Origami launcher. Emergent Scientist 3, 5. doi:10.1051/emsci/2019004, arXiv:1904.06409.

[13] Klett, Y., 2018. PALEO: Plastically Annealed Lamina Emergent Origami, in: Volume 5B: 42nd Mechanisms and Robotics Conference, ASME. p. V05BT07A062. doi:10.1115/DETC2018-85983.

[14] Lang, R.J., 2012. Origami Design Secrets: Mathematical Methods for an Ancient Art. 2nd ed.

[15] Lechenault, F., Thiria, B., Adda-Bedia, M., 2014. Mechanical response of a creased sheet. Physical Review Letters 112, 1–5. doi:10.1103/PhysRevLett.112.244301, arXiv:1404.1243.

[16] Liu, B., Silverberg, J.L., Evans, A.A., Santangelo, C.D., Lang, R.J., Hull, T.C., Cohen, I., 2018. Topological kinematics of origami metamaterials. Nature Physics , 1–5doi:10.1038/s41567-018-0150-8.

[17] López Jiménez, F., Pellegrino, S., 2012. Folding of fiber composites with a hyperelastic matrix. International Journal of Solids and Structures 49, 395–407. doi:10.1016/j.ijsolstr.2011.09.010.

[18] Lv, C., Krishnaraju, D., Konjevod, G., Yu, H., Jiang, H., 2015. Origami based Mechanical Metamaterials. Scientific Reports 4, 5979. doi:10.1038/srep05979.

[19] Mentrasti, L., Cannella, F., Pupilli, M., Dai, J.S., 2013. Large bending behavior of creased paperboard. II. Structural analysis. International Journal of Solids and Structures 50, 3097–3105. doi:10.1016/j.ijsolstr.2013.05.021.

[20] Nagasawa, S., Fukuzawa, Y., Yamaguchi, D., Nagae, S., Katayama, I., Yoshizawa, A., 2001. Deformation Characteristics on Creasing of Paperboard Under Shallow Indentation. arXiv:ICF10-0202-1-6.

[21] Nagasawa, S., Fukuzawa, Y., Yamaguchi, T., Tsukatani, S., Katayama, I., 2003. Effect of crease depth and crease deviation on folding deformation characteristics of coated paperboard. Journal of Materials Processing Technology 140, 157–162. doi:10.1016/S0924-0136(03)00825-2.

[22] Pradier, C., Cavoret, J., Dureisseix, D., Jean-Mistral, C., Ville, F., 2016. An Experimental Study and Model Determination of the Mechanical Stiffness of Paper Folds. Journal of Mechanical Design 138, 041401. doi:10.1115/1.4032629.

[23] Robinson, N., 2004. The Origami Bible: A Practical Guide to the Art of Paper Folding. Pavilion Books.

[24] Schenk, M., Guest, S.D., 2013. Geometry of Miura-folded metamaterials. Proceedings of the National Academy of Sciences 110, 3276–3281. doi:10.1073/pnas.1217998110.

[25] Silverberg, J.L., Na, J., Evans, A.A., Liu, B., Hull, T.C., Santangelo, C.D., Lang, R.J., Hayward, R.C., Cohen, I., 2015. Origami structures with a critical transition to bistability arising from hidden degrees of freedom. Nature materials 14, 389–93. doi:10.1038/nmat4232.

[26] Tachi, T., 2009. Simulation of Rigid Origami, in: Origami 4. A K Peters/CRC Press, pp. 175–187.

[27] Tachi, T., Hull, T.C., 2017. Self-Foldability of Rigid Origami. Journal of Mechanisms and Robotics 9, 021008. doi:10.1115/1.4035558.

[28] Thiria, B., Adda-Bedia, M., 2011. Relaxation mechanisms in the unfolding of thin sheets. Physical Review Letters 107, 1–4. doi:10.1103/PhysRevLett.107.025506.

[29] Tolley, M.T., Felton, S.M., Miyashita, S., Aukes, D., Rus, D., Wood, R.J., 2014. Self-folding origami: shape memory composites activated by uniform heating. Smart Materials and Structures 23, 094006. doi:10.1088/0964-1726/23/9/094006.

[30] Waitukaitis, S., Menaut, R., Chen, B.G.g., van Hecke, M., 2015. Origami Multistability: From Single Vertices to Metasheets. Physical Review Letters 114, 055503. doi:10.1103/PhysRevLett.114.055503, arXiv:1408.1607.

[31] Wei, Z.Y., Guo, Z.V., Dudte, L., Liang, H.Y., Mahadevan, L., 2013. Geometric mechanics of periodic pleated origami. Physical Review Letters 110, 1–5. doi:10.1103/PhysRevLett.110.215501, arXiv:1211.6396.